Autonomous Wideband Piezoelectric Energy Harvesting Utilizing a Resonant Inverter

Aaron L.F. Stein, and Heath Hofmann, *Senior Member, IEEE*

***Abstract*—Piezoelectric energy harvesters generate electrical power from ambient mechanical vibrations, making these vibrations a viable energy source for powering wireless sensor and identifier nodes. In order to harvest an appreciable amount of power, piezoelectric devices are typically inserted into high-Q mechanical resonant structures that significantly limit their harvesting bandwidth. The dynamic active energy harvesting method has been proposed as a way to widen the bandwidth of resonant piezoelectric energy harvesters; however, an autonomous design has not yet been demonstrated. This work demonstrates the first autonomous implementation of this method. This was accomplished through the use of a resonant inverter topology in combination with a low-power analog control circuit design that reduces the computational demand of the microcontroller. Experimental results using the Mide Volture V20w piezoelectric device shows that the harvested power is up to twice that of the adaptive rectifier method. These results include previously ignored loss mechanisms such as control losses, gating losses, and phase detection losses, making this system the first autonomous energy harvesting system of its kind.**

I. Introduction

RECENT advancements in low-power microelectronics have increased the viability and use of wireless sensor and identifier nodes. Currently these nodes are used in automobiles, heart monitoring, building environmental control, and many other applications [1]–[6]. Many of these nodes exist in environments that have limited electrical access, yet are in the presence of vibrations. In some applications ambient mechanical vibrations might be accessible, while in others the vibration could be created as part of an acoustic energy transfer system [7]. Either way, piezoelectric devices are a good choice for harvesting this energy because they have a large energy density and the output voltage is large enough to be useful in practical circuit designs [5], [7], [8]. In order to increase the electrical power extracted from the piezoelectric device to usable levels, it is common to incorporate the device into a high-Q mechanical resonator whose resonant frequency matches the excitation frequency.

Researchers have investigated many different electrical circuit topologies to maximize the energy harvested from resonant piezoelectric systems. Using the standard approach presented in [9], the piezoelectric device's voltage is rectified and applied to a load resistor and capacitor. In [9], the authors determined that an optimum load resistance can be found that maximizes the harvested power. In [10] a switching converter interfaces the rectifier and the load, so that the rectifier voltage can be controlled while allowing the harvested energy to be stored in a battery. Also in [10] it is demonstrated that an optimal rectifier voltage exists which is dependent on harvesting conditions. Operating at the optimal rectifier voltage exhibits a significant increase in power harvested. Despite the gains in this area rectifier-based approaches are limited in their power extraction ability.

Conventional rectifier-based approaches were enhanced by the introduction of the synchronized switch harvesting on inductor (SSHI) electronic interface. The parallel SSHI method utilizes a resonant transition to invert the voltage on the piezoelectric device [9], [11]. In [12], it is illuminated that the parallel SSHI circuit significantly outperforms the standard rectifier approach for weakly-coupled systems; however, for strongly coupled systems, the standard rectifier approach and the parallel SSHI topology harvest similar amounts of energy.

The active energy harvesting method applies a square wave voltage to the piezoelectric device. A thorough analysis of the active energy harvesting technique is presented in [13] and [14], and discussed in [15]. These articles use a pulse-width-modulated full-bridge inverter to implement the active energy harvesting method. Although control and gating losses were neglected, experimental results demonstrated in [14] that the active energy harvesting method outperforms the rectifier methods and SSHI technique in terms of energy harvested.

The active energy harvesting method is effective at harvesting energy when the mechanical resonant

This article has been accepted for publication in a future issue of this journal, but has not been fully edited. Content may change prior to final publication. Citation information: DOI 10.1109/TPEL.2016.2616301, IEEE Transactions on Power Electronics

frequency and excitation frequency are extremely close. However, the small bandwidth of a high-Q resonant mechanical structure means that deviations in the resonator frequency from the excitation frequency, for example due to mechanical parameter tolerances, can result in dramatically reduced harvesting levels. To mitigate this issue, researchers have proposed various mechanical techniques to increase the energy harvesting bandwidth [16]–[20]. For example, [20] utilizes a second piezoelectric device to provide stiffness tuning which adaptively tunes the mechanical resonant frequency. This method requires one piezoelectric device for energy harvesting and another one for actuation.

A detailed comparison of the bandwidth of the rectifier method and the SSHI method is discussed in [21]. The parallel SSHI method and the active energy harvesting methods provide some bandwidth extension over adaptive rectifier methods; however, neither method adapts to the changing harvesting conditions that occur as the excitation frequency deviates from the resonant frequency.

The dynamic active energy harvesting (DAEH) method presented in [22] is an electrical strategy for increasing the bandwidth, that adapts the electric circuitry in order to more effectively harvest energy at off-resonant frequencies. The high-Q mechanical system is modeled as a mass-spring-damper system, as illustrated in Fig. 1. Using this model for the energy harvesting system, [22] derives an optimal load impedance to maximize the power extracted from the device. The optimal load impedance is a function of system parameters, including the mechanical resonant frequency and the excitation frequency. Theoretically, applying the optimal load impedance to the piezoelectric device allows 100% of the available energy to be harvested over an infinite bandwidth; however, energy loss in the power electronics limit the practical bandwidth [22]. Using the dynamic active energy harvesting (DAEH) approach, [22] harvested up to 6 times as much energy at off-resonant frequencies when compared to the adaptive rectifier technique introduced in [10].

The benefits of the DAEH method were experimentally validated by [22]. However, the implementation was not an autonomous system, and the bandwidth improvements were modest due to the efficiency of the power electronics. The MOSFET gate drive, control circuitry, microcontroller, and phase detection power consumption exceeded that of the energy harvested, questioning the practical viability of the method. In this paper a resonant full bridge inverter topology is presented which, in combination with low-power analog control circuitry and low frequency digital control, reduces the loss mechanisms such that the practical benefits of the method are realized. In this work, experimental results of the dynamic active energy harvesting approach include all of the associated loss mechanisms, resulting in a wideband autonomous energy harvesting system.

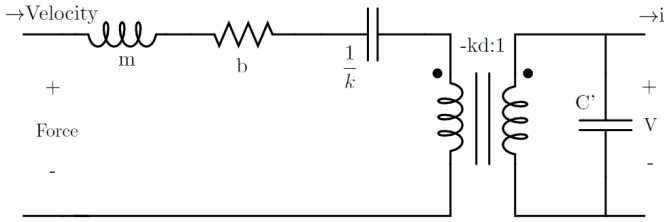

Fig. 1: Electric circuit model of a resonant mass-spring piezoelectric energy harvesting system.

This work significantly extends the work presented in our conference publication [23]. The new contributions in this article include:

- a demonstration of a fully autonomous implementation of the DAEH Method (including microprocessor power consumption),
- a theoretical loss analysis of the clamping event in the resonant inverter, and
- control circuitry that allows the inverter to freely operate without the microprocessor for a significant period of time.

II. Dynamic Active Energy Harvesting

A piezoelectric device used in a resonant mass-spring energy harvesting system can be modeled as shown in Fig. 1. The variables for this system are described in Table I. As discussed in [22], to maximize the power extracted from the piezoelectric device, impedance matching is used to derive the optimal load at a given vibration frequency ω,

$$\tilde{Z}_{opt} = \frac{\omega^2 m - k + j\omega b}{\omega^2 C' b - j\omega(\omega^2 C' m - (C' + d^2 k)k)}. \quad (1)$$

The optimal impedance shown in (1) has both real and imaginary components whose values change depending on harvesting conditions. Assuming a sinusoidal excitation force, this impedance can be emulated by applying a sinusoidal voltage whose

This article has been accepted for publication in a future issue of this journal, but has not been fully edited. Content may change prior to final publication. Citation information: DOI 10.1109/TPEL.2016.2616301, IEEE Transactions on Power Electronics

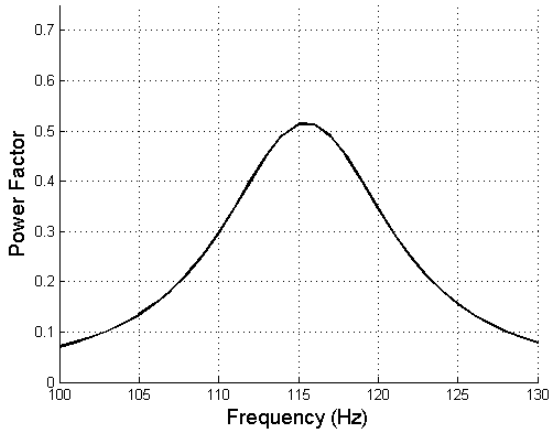

Fig. 2: The power factor of the optimal load impedance is plotted as a function of excitation frequency for the device parameters shown in Table I.

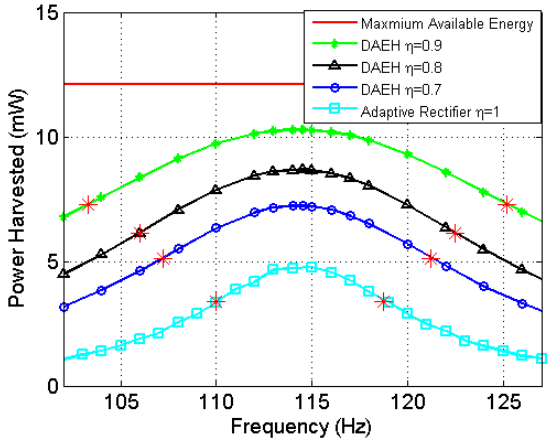

Fig. 3: The theoretical power harvested using the adaptive rectifier and the DAEH method is plotted as a function of excitation frequency for various power electronic efficiencies. The 3dB bandwidth of the harvested power is denoted by a red star. The device parameters used to generate this plot are shown in Table I.

magnitude is

$$V_{mag} = \sqrt{\omega^2 b^2 + (k - \omega^2 m)^2}\frac{F_m}{2kd\omega b}, \qquad (2)$$

and whose phase relative to the input force is

$$\phi = 180^\circ - \tan^{-1}\left(\frac{k - \omega^2 m}{\omega b}\right). \qquad (3)$$

Practical implementations of this method use a square wave voltage that matches the fundamental magnitude and frequency of the optimal sinusoid [22]. The efficiency of the power-path of the electronic inverter that applies such a square wave is crucial in maximizing the energy harvested over a wide bandwidth. The optimal load impedance has a reactive component that increases as the excitation frequency deviates from the mechanical resonant frequency. This trend is illustrated in Fig. 2. The inverter must therefore process both reactive and real power, so as the ratio of reactive power to real power increases at off-resonant frequencies, the impact of the inverter's power-path efficiency increases. It is important to note that, in practice, the efficiency of power electronic circuits will decrease at lower power factors. At off-resonant frequencies the power-path efficiency of the resonant inverter significantly affects the net harvested power. Using experimental device parameters from this work (shown in Table I), the effects of the power electronic's power-path efficiency on the DAEH method are shown in Fig. 3.

TABLE I: Volture V20w Piezoelectric Energy Harvesting System Parameters

Parameter	**Value**
Mass (m)	$6.7\ g$
Force Magnitude (F_m)	$0.218\ N$
Spring constant (k)	$3437\ \frac{N}{m}$
Damping coefficient (b)	$0.4960\ \frac{N*s}{m}$
Zero-strain capacitance (C')	$0.114\ \mu F$
Piezoelectric coupling (d)	$1.39\ \frac{\mu m}{v}$
Vibration period (T_m)	$8.2 - 9.4\ ms$

III. Resonant Inverter

To efficiently implement the square wave required by the DAEH method, a resonant full-bridge inverter is used, as depicted in Fig. 4. The proposed resonant inverter creates an efficient power electronic interface between the piezoelectric device and the bus capacitance. The resonant inverter is controlled such that the magnitude and the phase of the applied square wave can be modulated while undergoing only four switching transitions per voltage inversion. Unlike previous implementations, which used pulse-width-modulation (PWM) to transition the piezoelectric device voltage between $+V_{bus}$ and $-V_{bus}$ [13]–[15], [22], the proposed inverter topology uses the resonance of the piezoelectric capacitance (C') in combination with the inductance (L) to achieve the voltage transition. The resonant inverter utilizes

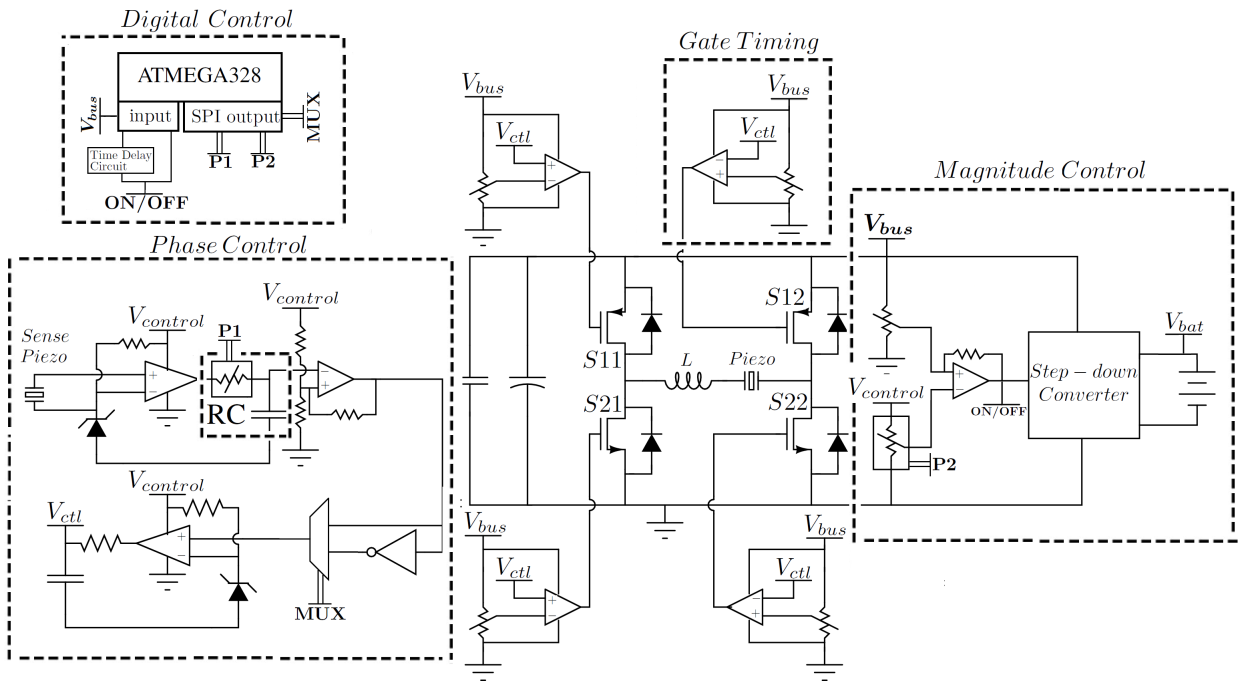

Fig. 4: Proposed resonant full-bridge inverter and analog control circuitry for implementing the dynamic active energy harvesting method. Note: potentiometers inside rectangular boxes are digital potentiometers.

the advantage of the SSHI method, using resonance to invert the piezoelectric voltage, while still providing a bi-directional converter capable of implementing the DAEH method. By drastically reducing the number of switching events required to transition the piezoelectric voltage, the resonant inverter topology nearly eliminates switching and gating losses. The resulting improvement in efficiency is one of the major reasons the autonomous wideband energy harvester is feasible.

A. The Resonant Transition

The proposed circuit topology inverts the piezoelectric device voltage while undergoing four switching transitions, which results in five circuit states. These states are exhibited in Fig. 5. To understand the resonant transition, an example voltage inversion is described.

Initially the piezoelectric device voltage is equal to V_{bus} as MOSFETs S_{11} and S_{22} are ON while MOSFETs S_{12} and S_{21} are OFF, as portrayed in Fig 5a. Turning S_{11} OFF (Fig. 5b) and then S_{21} ON (Fig. 5c) initiates a resonant transition between L and C'. Once the voltage across C' reaches its minimum and the inductor current returns to zero, switch S_{22} is opened (Fig. 5d), ending the resonant transition. The resulting voltage and current on the piezoelectric device are shown in Fig. 6. After the resonant transition the resulting voltage on the device, $-V_x$, is dependent both on the quality factor (Q_f) of the resonant transition, and the parasitic capacitance shown in Fig. 7.

Due to losses during the resonant transition, the resonant voltage inversion will be incomplete. The voltage on the piezoelectric device at the end of the resonant transition (V_{inv}) is

$$V_{inv} = V_{bus}\sqrt{1 - \frac{\pi}{Q_f}}. \tag{4}$$

Where the quality factor Q_f is determined by the energy lost energy lost during the resonant transition (E_{res}),

$$Q_f = \frac{\pi C' V_{bus}^2}{2E_{res}}. \tag{5}$$

V_{inv} is further reduced by the parasitic capacitances, C_{par}, across S22 and S12 that are created by both the MOSFET and the PCB layout. When the switch S22 opens, as shown in Fig. 5d, a series-connected LCC circuit is created with the parallel combination of the parasitic capacitances. Initially the parasitic capacitances have no charge. Once the network reaches steady state, the voltage on the piezoelectric

This article has been accepted for publication in a future issue of this journal, but has not been fully edited. Content may change prior to final publication. Citation information: DOI 10.1109/TPEL.2016.2616301, IEEE Transactions on Power Electronics

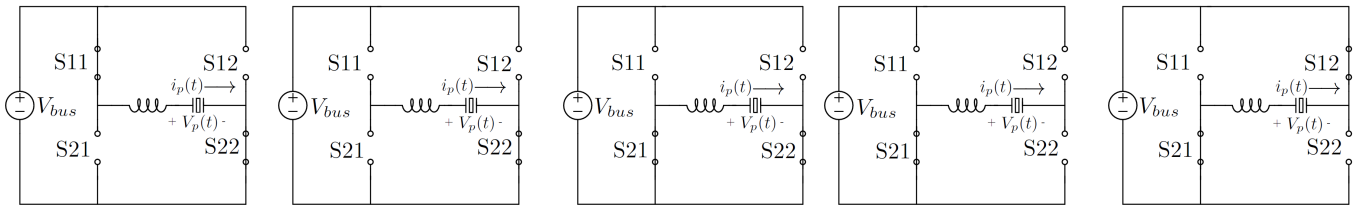

(a) Initial state (b) Open Circuit (c) Res. Transition (d) Open Circuit (e) Final State

Fig. 5: Required states for transitioning the piezoelectric device between the positive bus voltage and the negative bus voltage. To transition the device voltage between the negative bus voltage and the positive bus voltage, the states occur in reverse order.

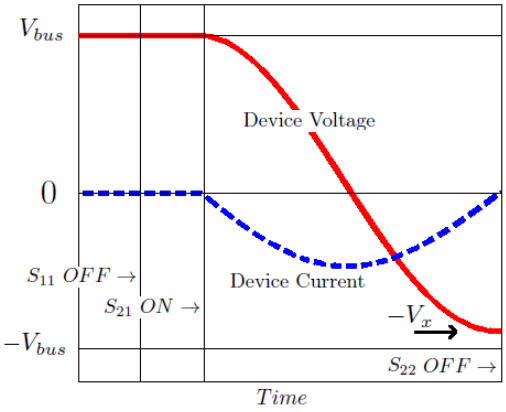

Fig. 6: The piezoelectric device voltage and current during a resonant voltage inversion.

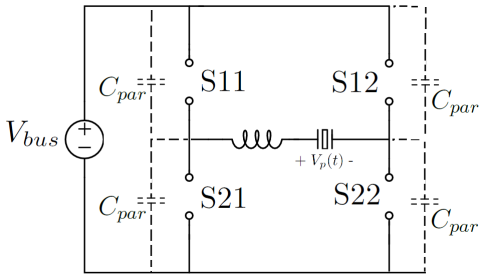

Fig. 7: Circuit model of the parasitic capacitances C_{par}. This capacitance models the effects of: the drain to source capacitances of the N-channel MOSFETs, P-channel MOSFETs, and PCB layout parasitic capacitance.

device is

$$V_x = V_{inv}\frac{C'}{C' + 2C_{par}}. \quad (6)$$

Two methods of transitioning the device voltage from $-V_x$ to $-V_{bus}$ are proposed in Section III-B.

B. Incomplete Voltage Inversion

The difference between the magnitude of the device voltage and bus voltage at the end of the resonant transition must be dealt with. Two methods for transitioning the device voltage to bus voltage after the resonant transition are:

- clamping the device and inductor to the bus voltage (shown in Fig. 8), or
- using the piezoelectric effect to charge the device capacitance until its voltage reaches the bus voltage (shown in Fig. 9).

The effectiveness of each method is determined by the total amount of energy that can be harvested from the piezoelectric device. During a half-cycle of the mechanical oscillation, the maximum energy that can be harvested, E_{ideal}, is determined by V_{bus} and the device current, $i_p(t)$. The available energy is

$$E_{ideal} = V_{bus}\left|\int_0^{\frac{Tm}{2}} i_p(t)dt\right| = V_{bus}Q_{ideal}. \quad (7)$$

The energy lost by either method is dependent on the magnitude of the voltage on the piezoelectric device at the end of the resonant transition, V_x.

1) Clamping: Clamping the piezoelectric device and resonant inductor to the bus voltage causes the piezoelectric device voltage to be a decaying oscillation centered around V_{bus}, as shown in Fig. 8. The energy extracted from the bus voltage during clamping, E_{ext}, is

$$E_{ext} = \int V_{bus}dq = V_{bus}\int_{V_x}^{V_{bus}} (C' + 2C_{par})dV_p$$
$$= (C' + 2C_{par})V_{bus}(V_{bus} - V_x). \quad (8)$$

After clamping the total energy (E_{ideal}) is harvested from the device. Therefore if the device is clamped to the bus capacitance, the net energy harvested to the bus, E_{clamp}, is

$$E_{clamp} = E_{ideal} - E_{ext}$$
$$= V_{bus}Q_{ideal} - (C' + 2C_{par})V_{bus}(V_{bus} - V_x). \quad (9)$$

This article has been accepted for publication in a future issue of this journal, but has not been fully edited. Content may change prior to final publication. Citation information: DOI 10.1109/TPEL.2016.2616301, IEEE Transactions on Power Electronics

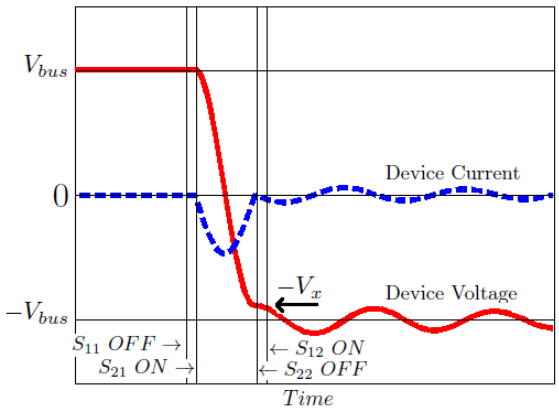

Fig. 8: The piezoelectric device voltage and current waveforms due to clamping after the resonant transition.

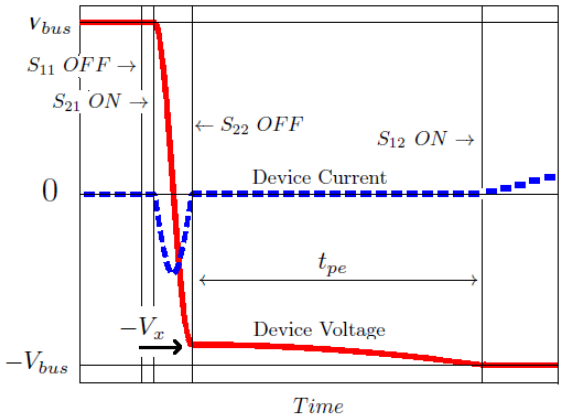

Fig. 9: The piezoelectric device voltage and current waveforms when using the piezoelectric effect to charge the device capacitance after the resonant transition.

2) Piezoelectric Effect: Using the piezoelectric effect to charge the piezoelectric device voltage to the bus voltage also reduces the amount of energy that can be harvested. During the charging interval (t_{pe}), the amount of charge supplied by the piezoelectric device, Q_c, to charge the device capacitance from V_x to V_{bus} is

$$Q_c = (C' + 2C_{par})(V_{bus} - V_x). \tag{10}$$

This charge must be subtracted from the ideal harvested charge; therefore, the energy that can be harvested while using the piezoelectric effect for charging, E_{pe}, is

$$E_{pe} = V_{bus}(Q_{ideal} - Q_c)$$
$$= V_{bus}Q_{ideal} - (C' + 2C_{par})V_{bus}(V_{bus} - V_x). \tag{11}$$

3) Comparison: The energy harvested when clamping the device, E_{clamp}, is the same as when using the piezoelectric effect to charge the device, E_{pe}. Therefore, the best method for railing the device voltage after the resonant transition is based on the implementation of the method rather than the method itself. In order to reduce the complexity of the switch timing, the clamping method was used in this work. However, for faster excitation frequencies it is possible that the ringing caused by clamping would not settle between resonant transitions. This could reduce the effectiveness of the subsequent resonant transition; therefore, the piezoelectric effect should be used instead of the clamping method in such circumstances.

C. MOSFET Timing

A practical implementation of the resonant inverter requires control over both the order of the switching and the timing associated with it. To achieve this a transition command signal, derived from the base accleration, is connected to a nanowatt comparator which drives an RC circuit between 0 and $V_{control}$. This portion of the circuit is highlighted in Fig. 4. As the voltage rises or declines across the capacitor in the RC circuit, it is compared to reference voltages associated with the proper switching order, as shown in Fig. 4. The switching order is symmetrical, so a single threshold for each switch will allow the inverter to reach both states.

The RC circuit is responsible for more than just the switch modulation order; it also must control the resonant transition. The time the circuit should be in the resonant state, shown in Fig. 5c, is half of the resonant period, and must be the same independent of whether the RC network is charging or discharging. In order to accomplish this, the threshold voltages for S_{21} and S_{22} are chosen symmetrically on either side of $\frac{V_{control}}{2}$:

$$V_{S21} = \frac{V_{control}}{2} - \frac{V_{control}\left(e^{\frac{\pi\sqrt{LC'}}{RC}} - 1\right)}{2\left(e^{\frac{\pi\sqrt{LC'}}{RC}} + 1\right)} \tag{12}$$

and

$$V_{S22} = \frac{V_{control}}{2} + \frac{V_{control}\left(e^{\frac{\pi\sqrt{LC'}}{RC}} - 1\right)}{2\left(e^{\frac{\pi\sqrt{LC'}}{RC}} + 1\right)}. \quad (13)$$

Unlike S_{21} and S_{22}, the timing of S_{11} and S_{12} do not affect the resonant transition; however, to minimize losses they should be switched immediately before and after the resonant transition. As discussed in section III-B3, either clamping or using the piezoelectric effect to charge the device capacitance after the resonant transition results in the same amount of harvested power. However, using the RC network to control the MOSFET timing means that, if clamping is delayed (Fig. 5d), then when the transition command triggers the next voltage inversion there will be a delay once the inverter is open-circuited (Fig. 5b). During this time the piezoelectric effect will start to discharge the piezoelectric capacitance. This reduces the effectiveness of the resonant transition and should therefore be avoided.

IV. Circuit Control

The DAEH method emulates the optimal load impedance by modulating the phase and magnitude of the applied square wave with respect to the applied force. In order to adjust to changing conditions, a peak power tracking algorithm dynamically modulates these parameters to maximize the energy harvested. Previous implementations such as [22], [23], relied on high-power digital circuitry to achieve the required control. In order to achieve an autonomous energy harvesting system, a reduction of the digital computation demand was achieved by implementing high-frequency (e.g., greater than 5Hz) tasks with low-power analog circuitry.

1) Phase Control: In practice, the phase of the resonant inverter is adjusted relative to the zero crossing of the base mechanical acceleration. A low-power acceleration polarity detector was created using a sense-piezoelectric device. The sense-piezoelectric device is clamped in parallel with the main device, and is small so as to not interfere with the mechanical dynamics of the main device. The output voltage of the sense-piezoelectric device is proportional to the base acceleration. Using a differential comparator, a reference square wave is generated whose transitions align with the zero-crossing of the base mechanical acceleration.

The phase-shifted signal is created by applying a time delay to the reference square wave. The time delay is generated by passing the reference square wave through an RC filter whose time constant is set by a digital potentiometer. A hysteresis comparator generates a time-delayed square wave from the first-order RC response. The maximum time delay that can be achieved by this circuit is one-half of the square wave period (180°). In order to achieve a full 360° phase shift, the time-delayed square wave is inverted using a NOT gate. A multiplexer is used to select between the inverted and the original time-delayed square wave. The phase control circuit is illustrated in Fig. 4. This circuit produces the transition command signal, yet in steady-state it does not require microprocessor input, which greatly reduces the power consumption of the digital control.

2) Analog Magnitude Control: The magnitude of the square wave voltage applied to the device by the inverter is determined by the bus voltage, V_{bus}. The bus voltage is controlled using an analog hysteresis controller which connects a DC-DC converter load when the bus voltage is above the upper threshold, and disconnects it when the bus voltage is below the lower threshold. This control circuit is also illustrated in Fig. 4. The hysteresis controller allows the harvested power to be measured, which is necessary for the peak power tracker. This process is discussed in Section IV-3.

3) Digital Control: The digital control in this work is implemented on an ATMEGA328 microcontroller with a clock frequency of 62.5KHz; however, in a practical energy harvesting system for wireless sensor nodes, the microcontroller used to implement the node itself could be used to control the energy harvesting system. The microcontroller is responsible for implementing the peak-power-tracking algorithm by changing the phase and magnitude of the applied square wave, yet its power consumption must be minimal in order to achieve an autonomous design. This is accomplished by designating the high-frequency tasks to analog circuitry so that the microprocessor can be in a more efficient state (sleep mode), as described in sections IV-1 and IV-2. The digital control interfaces with the analog circuitry through two digital potentiometers and a multiplexer. Modulation of these allows the microcontroller to change the magnitude and phase of the applied square wave; however, it does not require the micocontroller to be awake in order to

maintain the current phase and magnitude.

A peak-power-tracking algorithm, similar to that in [22], is used to find the optimum bus voltage and phase angle with one modification. The algorithm is shown in Table II. In order to reduce power consumption, the net power harvested is computed by measuring the voltage on the bus capacitance at the beginning of the magnitude control hysteresis cycle (discussed in Section IV-2), and after a delay t_{delay}. Therefore the average power harvested, $P_{harvest}$, is measured passively during each magnitude control hysteresis cycle.

$$P_{harvest} = \frac{\frac{1}{2}C_{bus}[V_{bus}(t_{delay})^2 - V_{bus}(0)^2]}{t_{delay}} \quad (14)$$

In order to minimize power consumption, the microcontroller is in a "sleep" mode except when triggered by external interrupts at the appropriate time to measure the bus voltage. During each hysteresis cycle either the harvested power is measured, the bus voltage magnitude is perturbed, or the phase angle is perturbed.

TABLE II: Digital Control: Peak-Power-Tracking Algorithm [22]

Hysteresis Cycle	Execution
1	Measure Power (P1)
2	$V_{bus} = V_{bus} + \Delta V_{bus}$
3	Measure Power (P2)
4	if (P1>P2) : $V_{bus} = V_{bus} - 2\Delta V_{bus}$
5	Measure Power (P1)
6	$\phi = \phi + \Delta\phi$
7	Measure Power (P2)
8	if (P1>P2) : $\phi = \phi - 2\Delta\phi$
REPEAT	Go to 1

The length of the magnitude-control hysteresis cycle therefore determines the power consumption of the microcontroller. The longer the hysteresis cycle, the less power that is consumed by the microcontroller because the ratio of sleep to awake time increases. However, this decrease in power consumption comes at the cost of increased time required to converge to the optimal harvesting conditions.

4) Startup Control: One of the benefits of using low-power analog control circuitry to implement high-frequency tasks is that it aids in the startup process. The startup process has three different modes.

First, when the voltage on the bus capacitance is less than the minimum voltage required for the control circuitry, all of the switches in the inverter are OFF. This results in the piezoelectric device charging the device capacitance through a full-bridge rectifier consisting of the body diodes in the MOSFETs.

Next, once the voltage of the bus capacitance is large enough to turn on the control circuitry, the microprocessor runs an initiation sequence that sets the digital potentiometers for the analog phase and magnitude control circuits. At this point a square voltage wave is applied to the piezoelectric device in phase with the applied force.

Finally, once the voltage on the bus capacitance is large enough to trigger the analog magnitude control, the peak power tracking algorithm begins to dynamically search for the optimal harvesting conditions.

V. Results

Experimental results were obtained using a Mide Volture V20w piezoelectric device with a 6.7 g tip mass. The adaptive rectifier and DAEH harvesting methods were applied to the device over a frequency range of 106-122 Hz. The resonant frequency of the piezoelectric device is higher than the data-sheet suggests due to our custom clamping mechanism, which shortens the effective length of the device . For consistency, the magnitude of the base acceleration was held constant at 32.5 $\mathrm{m\,s^{-2}}$ for all experiments. The piezoelectric device parameters, shown in Table I, were calculated based on the short-circuit and open-circuit resonant frequencies of the piezoelectric device [24], [25].

A. Resonant Inverter

An experimental implementation of the resonant inverter was developed to demonstrate its performance and validate the design equations presented in Section III. The components chosen for the resonant inverter are listed in Table III. In order to achieve the bandwidth extension goals of this work, it is important to maximize the efficiency of the resonant inverter; therefore, the circuit losses are catalogued and discussed in this section. A breakdown of the major loss mechanisms is shown in Table IV and discussed in subsequent sections.

In order to accurately catalog the losses in the resonant inverter, the piezoelectric device is replaced

with a 125 nF film capacitor. The capacitor approximates the C' of the device, but does not have the electromechanical coupling of the piezoelectric device, which makes it easier to catalog the performance of the circuitry. The high efficiency of the film capacitor does not allow the oscillations from the clamping event to reach steady state between resonant transitions when operated at 114 Hz. Therefore the losses are measured at an excitation frequency of 10 Hz, and scaled up to 114 Hz.

TABLE III: Main Circuit Components

Component	**Part Numnber**
N-channel MOSFET	TI CSD18504Q5A
P-channel MOSFET	AO AOD413A
Comparator	LT LTC1540
Inductor Core	Ferroxcube RM10/LP-3F3
Inductance	2.8 mH
Inductor Turns	77
Inductor Gap	0.1 mm

TABLE IV: Catalogued losses for the resonant inverter generating a 10 V square wave at 10 Hz. These losses were scaled to 114 Hz to estimate the power consumption of the resonant inverter.

Loss Mechanism	**Loss at 10** Hz
Resonant / Clamping(E_{clamp})	1.4 µJ per transition
Gating (E_{gate})	0.32 µJ per transition
Quiescent Gate Circuit (P_{gd})	12.0 µW
MOSFET Leakage (P_{leak})	20.0 µW
Gate timing Potentiometers(P_{pot})	36.0 µW
Total	102.4 µW

1) Resonant Transition Losses: The most important loss mechanisms in the resonant inverter are losses that occur during the resonant transition. This is because, as shown in (9), losses during the resonant transition are also responsible for clamping losses. Careful measurement of the resonant period (T_e), the inductance (L), the device capacitance (C'), and the device voltage (V_p) are used to compute the energy in the system at the beginning and end of the resonant transition. Using a 10 V bus, the energy in the system at the beginning of the resonant transition, E_{init}, is found to be

$$E_{init} = \frac{1}{2}C'V_{bus}^2 = 6.25\mu J. \tag{15}$$

After the resonant transition the energy remaining in the system is given by

$$E_x = \frac{1}{2}C'V_x^2 = 5.88\mu J. \tag{16}$$

Experimental data shows that 0.37 µJ was lost during the resonant transition, therefore the resulting quality factor, which can be derived from (5), is 53.13. Using (6) the experimental quality factor predicts the V_{inv} to be 9.7 V, which was confirmed experimentally.

2) Clamping Losses: After the resonant transition, V_{inv} is further reduced by the parasitic capacitance C_{par}. This capacitance encompasses the parasitic capacitance of the MOSFET, parallel diode, and PCB parasitic capacitances. The measured capacitance is 5.75 nF, which based on (6) suggests that V_x will be 8.89 V; however, the experimental V_x was measured to be 9 V. The clamping losses E_{clamp} given by (9) are therefore 1.4 µJ per resonant transition.

3) Gate Drive Circuitry and MOSFET Leakage: Four LTC 1540 comparators are used to both generate the proper switch timing, and drive the gates of the MOSFETs. The losses in the gate drive circuitry fall into two categories.

First, the gating control circuitry has a quiescent power draw that is computed directly from the LTC1540 datasheet. The quiescent current draw for each comparator is 300 nA at 10 V which results in 12 µW of power consumption denoted by (P_{gd}). Next, the power dissipated by the potentiometers which control the gate timing P_{pot} consume $\frac{4V_{ctl}^2}{R_{pot}}$, which results in 36 µW of loss. Finally, the comparator sources $Q_{gs}V_{bus}$ joules every time a MOSFET turns on. During each resonant inversion 2 MOSFETs turn on; therefore, the energy lost to gating is $E_{gate} = 2Q_{gs}V_{bus} = 0.32\mu J$.

The MOSFET leakage current is approximately 1 µA. There are two conduction paths and the voltage across the MOSFET is 10 volts; therefore the leakage current causes 20 µW of power dissipation denoted by (P_{leak}).

4) Total Power Consumption of the resonant inverter: The total losses in the inverter can be computed based on the excitation frequency of the resonant inverter f_s. The energy lost during a resonant transition is independent of the excitation frequency of the inverter due to the time-scale separation. Therefore the power loss in the resonant transition

scales linearly with the excitation frequency, while the control circuitry represents a constant power draw. The total power loss in the inverter is therefore

$$P_{total} = 2f_s(E_{clamp} + E_{gate}) + P_{gd} + P_{leak} + P_{pot}. \quad (17)$$

At 10 Hz the total power consumption of the resonant inverter is calculated to be 102.4 µW. Experimental results found the total power consumption of the inverter to be 106.42 µW, which demonstrates less than a 4% error when compared to the calculated results. In order to measure the total power consumption, the bus capacitance was charged to 10.1 V. The voltage on the bus capacitance declined as power was consumed by the resonant inverter. The time it took for the voltage on the bus capacitance to decay to 10 V was measured and used to determine the losses in the inverter.

Based on (17) the resonant inverter power loss using a high-efficiency film capacitor at 114 Hz is estimated to be 460.2 µW.

5) Efficiency impact of the Piezoelectric Device: Experimental data shows that when a displacement-constrained Mide V20W piezoelectric device is driven with the resonant inverter the power consumption is 656 µW at 114 Hz. Assuming the behavior of the electrical circuit is unchanged when switching from the film capacitor to the piezoelectric device, the piezoelectric device is responsible for dissipating 195 µW.

The piezoelectric device impacts the energy lost in the inverter circuitry by adding additional loss to the resonant transition. Using the piezoelectric device, the resonant transition has a quality factor of 20.45, which results in 2.15 µJ per transition being dissipated. The piezoelectric device voltage and current during the resonant transition are shown in Fig. 10. At 114 Hz this results in an additional 171 µW of power dissipation. Therefore, the expected power dissipation is 631 µW. This has a 3% error when compared to the cumulative experimental loss data. One possible source is the electromechanical energy conversion of the device. Despite being clamped, the piezoelectric device still generates some mechanical power, which was observed from audible noise emanating from the device.

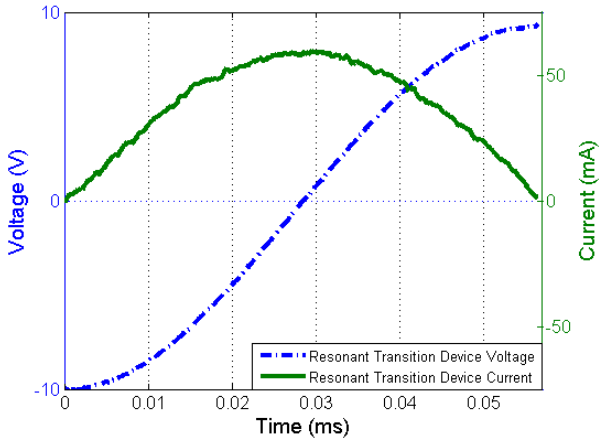

Fig. 10: Experimental piezoelectric device voltage and current waveforms during a resonant transition when V_{bus} is 10 V.

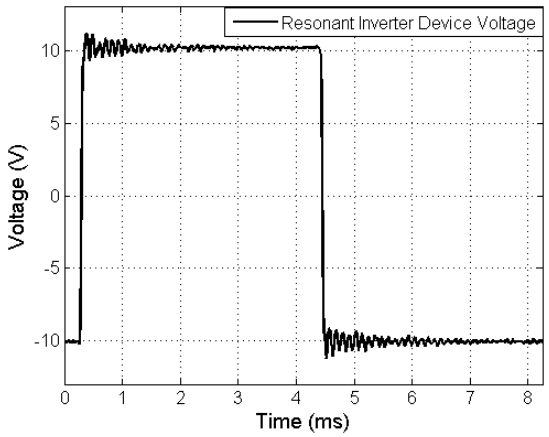

Fig. 11: Experimental piezoelectric device voltage waveform are shown for the case when V_{bus} is 10 volts.

B. Resonant Inverter Bandwidth Extension Capabilities

Careful consideration in the design of the resonant inverter was given to minimizing losses so that the bandwidth of the dynamic active energy harvesting (DAEH) method can be improved. To demonstrate the performance of the proposed resonant inverter, two energy harvesting methods were compared on an experimental setup: the adaptive rectifier method and the DAEH method utilizing the resonant inverter.

The adaptive rectifier circuit is used as a baseline for comparison, and is operated using the harvesting method described in [10]. The rectifier was made from Comchip CDBA140-G diodes, due to their low forward voltage. In order to present the adaptive rectifier method in the best possible light, all control circuitry for the adaptive rectifier was externally powered.

The resonant inverter was implemented with the

This article has been accepted for publication in a future issue of this journal, but has not been fully edited. Content may change prior to final publication. Citation information: DOI 10.1109/TPEL.2016.2616301, IEEE Transactions on Power Electronics

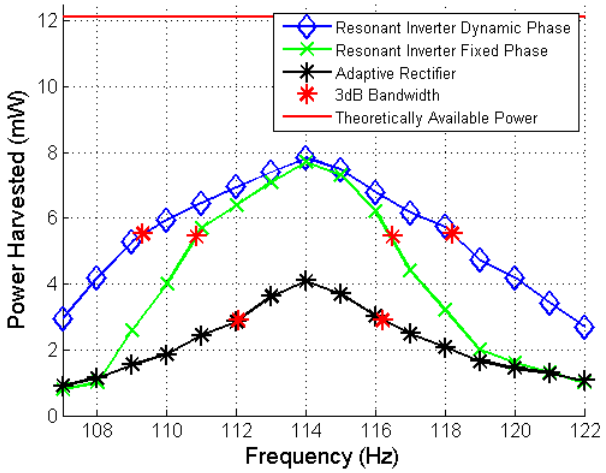

Fig. 12: The power harvested versus excitation frequency is illustrated with the DAEH method utilizing the resonant inverter, the adaptive rectifier method, and the resonant inverter with a fixed phase. To elucidate the capabilities of the resonant inverter, the circuitry is controlled using an externally powered accelerometer, control circuitry, and microprocessor in this comparison.

elements shown in Table III. To demonstrate the capabilities of the power electronics, the resonant inverter was used in a similar manner to the PWM full-bridge inverter presented in [22]. The control circuitry, including an accelerometer, was externally powered; however, the inverter loss mechanisms detailed in Table IV were included. The experimental device voltage waveform is shown in Fig. 11, and the power harvested from the resonant inverter is shown in Fig.12.

The DAEH method with the resonant inverter shows dramatic performance improvements over the adaptive rectifier approach, as shown in Fig.12. When the mechanical resonant frequency and the excitation frequency are close, the DAEH method with the resonant inverter harvests nearly twice as much power as the adaptive rectifier approach. As the excitation frequency deviates from the resonant frequency of the mechanical structure, the adaptive rectifier's harvested power falls off more quickly. The DAEH method with the resonant inverter harvests up to 2.63 times as much power at off-resonant frequencies, and increases the 3 db power bandwidth by a factor of 2.84.

In order to demonstrate the benefit of dynamic phase modulation, the phase of the applied square wave was fixed at an angle which maximizes the power harvested when the mechanical resonant frequency and the excitation frequency are the same. When operated with a fixed phase, the proposed energy harvesting system has similar device waveforms as both the SSHI method and the active energy harvesting method. As illustrated in Fig.12, the fixed-phase active energy harvesting method harvests a similar amount of power as the DAEH method when the excitation frequency and the mechanical resonant frequency are close; however, as the excitation frequency deviates from the mechanical resonant frequency, the DAEH method significantly outperforms the fixed-phase active energy harvesting method.

C. Autonomous System

This section demonstrates the dynamic active energy harvesting method on an autonomous system. The power extracted from the piezoelectric device is shown over an excitation frequency range of 106-122 Hz in Fig. 13. The total power harvested from the piezoelectric device onto the bus capacitance is shown as the harvested power. The net power harvested is the power harvested to the bus capacitance minus the control losses.

The control losses include both the analog circuitry and the microcontroller. The control losses varied between 1.9 and 2.37 mW, depending on the harvested power. The analog control circuitry consumes 178.3 $\mu\mathrm{W}$ in steady-state (i.e., when the digital state is not altered); therefore, the microcontroller dominates the control losses. The analog control circuitry comprises up to 7.5% of the control losses.

The current implementation of the digital controller generally settles on the optimal harvesting conditions in tens of seconds; however, the settling time is dependent on the amount of power being harvested. Small excitation levels, or large deviations between the mechanical resonant frequency and the excitation frequency, reduces the frequency of the magnitude controller, which slows the settling time of the digital controller. The proposed control algorithm is designed to accommodate deviations in the mechanical resonant frequency and the excitation frequency due to mechanical parameter tolerances, and therefore the settling time is not a design constraint.

This article has been accepted for publication in a future issue of this journal, but has not been fully edited. Content may change prior to final publication. Citation information: DOI 10.1109/TPEL.2016.2616301, IEEE Transactions on Power Electronics

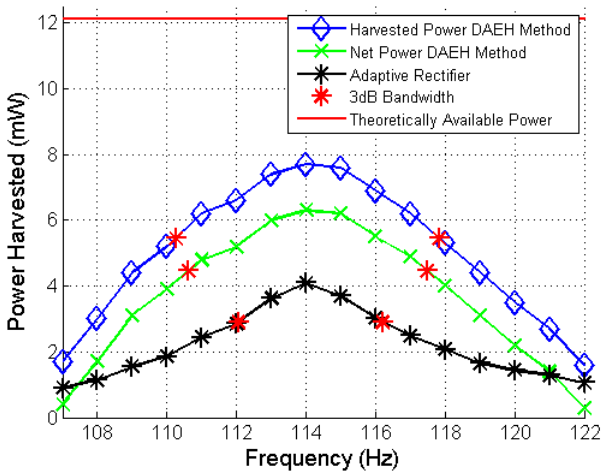

Fig. 13: The net power harvested versus excitation frequency by the autonomous energy harvesting system is shown with a green X. It is the total power harvested (shown with blue diamonds) minus the control losses, and is compared to the baseline adaptive rectifier approach (shown with black *). The net power harvested using the DAEH method includes all associated loss mechanisms including the microprocessor, while the adaptive rectifier method uses externally powered control circuitry.

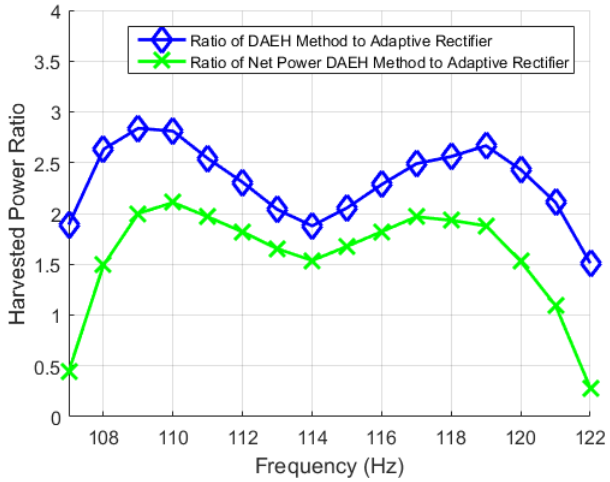

Fig. 14: Ratio of the power harvested using the DAEH method to the adaptive rectifier method (blue diamonds) and the ratio of the net power harvested using the DAEH method to the adaptive rectifier method (green X) is plotted versus excitation frequency.

The net power harvested from the DAEH method is 1.53 times more than the adaptive rectifier approach when the excitation frequency and mechanical resonant frequency are similar. As the excitation frequency deviates from the mechanical resonant frequency, the net power harvested with the DAEH method is up to 2.1 times more than the adaptive rectifier approach. Furthermore, the 3dB bandwidth of the net power harvested from the DAEH method is 1.65 times larger than the adaptive rectifier approach. A comparison between energy harvested from the DAEH method and the adaptive rectifier approach is illustrated in Fig. 14. This represents a conservative estimate of the gains of the proposed harvesting system, because no control losses were included with the adaptive rectifier approach. Given a practical implementation of the adaptive rectifier, the benefits of the proposed autonomous implementation of the DAEH method would be even more significant.

VI. Conclusion

In this paper a resonant inverter is presented which implements the dynamic active energy harvesting method while reducing switching losses and gating losses. The resonant inverter, in conjunction with new analog circuitry which implements the high-frequency control tasks required by the DAEH method, produces the first autonomous dynamic active energy harvesting system. When the excitation frequency and mechanical resonant frequency are similar, this system harvests 1.5 times more power than the adaptive rectifier approach, which is externally powered to maximize performance. As the excitation frequency deviates from the mechanical resonant frequency the proposed autonomous system harvests up to 2.1 times more power than the adaptive rectifier approach, and the resulting 3dB bandwidth of the system is 1.65 times larger. The demonstrated resonant inverter and control circuitry represent the first autonomous implementation of the dynamic active energy harvesting method for piezoelectric devices. This autonomous system increases the practical viability of using piezoelectric devices to power wireless sensor and identifier nodes by increasing their bandwidth and peak energy harvesting capabilities.

Future work in this area could focus on implementing the control circuitry for the DAEH method on an integrated circuit. This would significantly reduce power consumption and allow the DAEH method to be implemented at lower power levels.

REFERENCES

[1] I. F. Akyildiz, W. Su, Y. Sankarasubramaniam, and E. Cayirci, "Wireless sensor networks: a survey," *Computer networks*, vol. 38, no. 4, pp. 393–422, 2002.

[2] R. Tashiro, N. Kabei, K. Katayama, E. Tsuboi, and K. Tsuchiya, "Development of an electrostatic generator for a cardiac pacemaker that harnesses the ventricular wall motion," *Journal of Artificial Organs*, vol. 5, no. 4, pp. 0239–0245, 2002.

[3] P. D. Mitcheson, E. M. Yeatman, G. K. Rao, A. S. Holmes, and T. C. Green, "Energy harvesting from human and machine motion for wireless electronic devices," *Proceedings of the IEEE*, vol. 96, no. 9, pp. 1457–1486, 2008.

[4] J. Tavares, F. Velez, and J. Ferro, "Application of wireless sensor networks to automobiles," *Measurement Science Review*, vol. 8, no. 3, pp. 65–70, 2008.

[5] S. Roundy, P. K. Wright, and J. Rabaey, "A study of low level vibrations as a power source for wireless sensor nodes," *Computer communications*, vol. 26, no. 11, pp. 1131–1144, 2003.

[6] S. Rajeswari, "Energy harvesting cardiac pacemaker," Ph.D. dissertation, California State University, Northridge, 2015.

[7] M. G. Roes, J. L. Duarte, M. A. Hendrix, E. Lomonova *et al.*, "Acoustic energy transfer: a review," *Industrial Electronics, IEEE Transactions on*, vol. 60, no. 1, pp. 242–248, 2013.

[8] J. A. Paradiso and T. Starner, "Energy scavenging for mobile and wireless electronics," *Pervasive Computing, IEEE*, vol. 4, no. 1, pp. 18–27, 2005.

[9] A. Badel, D. Guyomar, E. Lefeuvre, and C. Richard, "Piezoelectric energy harvesting using a synchronized switch technique," *Journal of Intelligent Material Systems and Structures*, vol. 17, no. 8-9, pp. 831–839, 2006.

[10] G. K. Ottman, H. F. Hofmann, A. C. Bhatt, and G. A. Lesieutre, "Adaptive piezoelectric energy harvesting circuit for wireless remote power supply," *Power Electronics, IEEE Transactions on*, vol. 17, no. 5, pp. 669–676, 2002.

[11] A. Badel, A. Benayad, E. Lefeuvre, L. Lebrun, C. Richard, and D. Guyomar, "Single crystals and nonlinear process for outstanding vibration-powered electrical generators," *Ultrasonics, Ferroelectrics and Frequency Control, IEEE Transactions on*, vol. 53, no. 4, pp. 673–684, 2006.

[12] Y. Shu, I. Lien, and W. Wu, "An improved analysis of the sshi interface in piezoelectric energy harvesting," *Smart Materials and Structures*, vol. 16, no. 6, p. 2253, 2007.

[13] Y. Liu, G. Tian, Y. Wang, J. Lin, Q. Zhang, and H. F. Hofmann, "Active piezoelectric energy harvesting: general principle and experimental demonstration," *Journal of Intelligent Material Systems and Structures*, vol. 20, no. 5, pp. 575–585, 2009.

[14] E. Lefeuvre, G. Sebald, D. Guyomar, M. Lallart, and C. Richard, "Materials, structures and power interfaces for efficient piezoelectric energy harvesting," *Journal of electroceramics*, vol. 22, no. 1-3, pp. 171–179, 2009.

[15] M. Deterre, E. Lefeuvre, and E. Dufour-Gergam, "An active piezoelectric energy extraction method for pressure energy harvesting," *Smart Materials and Structures*, vol. 21, no. 8, p. 085004, 2012.

[16] S. Roundy, E. S. Leland, J. Baker, E. Carleton, E. Reilly, E. Lai, B. Otis, J. M. Rabaey, P. K. Wright, and V. Sundararajan, "Improving power output for vibration-based energy scavengers," *Pervasive Computing, IEEE*, vol. 4, no. 1, pp. 28–36, 2005.

[17] E. S. Leland and P. K. Wright, "Resonance tuning of piezoelectric vibration energy scavenging generators using compressive axial preload," *Smart Materials and Structures*, vol. 15, no. 5, p. 1413, 2006.

[18] Z. Yang and J. Yang, "Connected vibrating piezoelectric bimorph beams as a wide-band piezoelectric power harvester," *Journal of Intelligent Material Systems and Structures*, vol. 20, no. 5, pp. 569–574, 2009.

[19] G. K. Fedder, C. Hierold, J. G. Korvink, O. Tabata, O. Brand, I. Dufour, S. Heinrich, and F. Josse, *Resonant MEMS: Fundamentals, Implementation, and Application*. John Wiley & Sons, 2015.

[20] M. Lallart, S. R. Anton, and D. J. Inman, "Frequency self-tuning scheme for broadband vibration energy harvesting," *Journal of Intelligent Material Systems and Structures*, 2010.

[21] I. Lien, Y. Shu, W. Wu, S. Shiu, and H. Lin, "Revisit of series-sshi with comparisons to other interfacing circuits in piezoelectric energy harvesting," *Smart Materials and Structures*, vol. 19, no. 12, p. 125009, 2010.

[22] C. Luo and H. F. Hofmann, "Wideband energy harvesting for piezoelectric devices with linear resonant behavior," *Ultrasonics, Ferroelectrics and Frequency Control, IEEE Transactions on*, vol. 58, no. 7, pp. 1294–1301, 2011.

[23] A. Stein and H. Hofmann, "Resonant inverter design for stand-alone dynamic active piezoelectric energy harvesting," in *Applied Power Electronics Conference and Exposition (APEC), 2015 IEEE*. IEEE, 2015, pp. 3265–3271.

[24] N. Kong, D. S. Ha, A. Erturk, and D. J. Inman, "Resistive impedance matching circuit for piezoelectric energy harvesting," *Journal of Intelligent Material Systems and Structures*, 2010.

[25] E. Lefeuvre, A. Badel, C. Richard, L. Petit, and D. Guyomar, "A comparison between several vibration-powered piezoelectric generators for standalone systems," *Sensors and Actuators A: Physical*, vol. 126, no. 2, pp. 405–416, 2006.

Aaron L.F. Stein Aaron L.F. Stein received the Ph.D. degree in electrical engineering and computer science from the University of Michigan, Ann Arbor, MI, USA, in 2016. He is currently a Post-Doctoral Research Associate at Dartmouth College, Hanover, NH, USA. His research interests include power electronics, energy harvesting, wireless power transfer, and magnetic components of power electronic circuits.

Heath F. Hofmann Heath F. Hofmann (M'92, SM'16) received the Ph.D. degree in electrical engineering and computer science from the University of California at Berkeley, Berkeley, CA, USA, in 1998. He is currently an Associate Professor with the University of Michigan, Ann Arbor, MI, USA. He has authored approximately 40 papers in refereed journals and holds 13 patents. His current research interests include power electronics, specializing in the design, simulation, and control of electromechanical systems, adaptive control techniques, energy harvesting, flywheel energy storage systems, electric and hybrid electric vehicles, and finite-element analysis.